

Modeling Acoustic Attenuation, Sound Velocity and Wave Propagation in Lithium-Ion Batteries via a Transfer Matrix

Simon Feiler,^[a] Lukas Gold,^[a] Sarah Hartmann,^[a] and Guinevere A. Giffin^{*[a, b]}

A simple 1D transfer matrix model of a battery is introduced and parametrized using harvested individual cell components at 0% and 100% SoC. This model allows for the calculation of group velocity and attenuation. The results of the model show good agreement with measured values, highlighting increased attenuation and group velocity at the resonances. This emphasizes the importance of selecting a suitable interrogation frequency for ultrasound investigations in lithium-ion batteries. The model accurately replicates the observed weakening of

resonances with increasing SoC. Additionally, it provides the basis to fit US spectroscopy data in the future, enabling immediate determination of component thickness and the Young's modulus of individual components, along with aiding in the identification aging effects of the anode and cathode materials. The model can visualize wave propagation within the battery. At certain frequencies, standing waves form which could be used in high-intensity ultrasound applications targeted at individual cell components.

Introduction

There is a growing interest in utilizing ultrasound as a nondestructive diagnostic tool to examine lithium-ion batteries (LIBs). There are two measurable quantities: the time of flight (ToF) and the amplitude of the wave passing through the battery. The ToF provides information about the stiffness (Young's modulus) and the speed of sound in the materials, rendering it sensitive to the transition of the active materials during charging,^[1–3] to film formation such as the solid electrolyte interphase (SEI) and lithium plating during aging.^[4–7] The amplitude contains information about absorption, resonances and other attenuating effects. Utilizing amplitude measurements has been effective in detecting gassing^[8] and plating.^[9] However, careful selection of the interrogation frequency is necessary due to the layered structure of batteries, which result in the emergence of band gaps, sometimes referred to as resonances or resonant reflections. In the vicinity of these band gaps, significant anomalies arise in the sound velocity and attenuation. Wasylowski et al.^[10] observed deformed reflected pulses, likely due to the dispersion near band gaps. Gold et al.^[11] measured discontinuities in sound velocity at different

frequencies, also likely caused by band gaps. Acoustic resonances in LIBs were described by Huang et al.,^[12] who concluded that echo measurements carry information through the layering distance and sound velocities of individual layers, potentially allowing the number of layers contained in a cell to be inferred. They also introduced a theoretical model (treating electrodes as a dense slurry and separators as porous liquid filled solids using the Biot model) to explain the wave physics within each layer and the formation of ultrasonic resonance from interlayer reflections by the summation of all individual reflections and transmissions. Similar treatment of the reflections and transmission can be achieved with the transfer matrix formalism which has already shown to effectively reproduce results from US measurements. E.g., Wang et al.^[13] successfully utilized a transfer matrix to reproduce the reflection angle spectrum, demonstrating the method's capability to model acoustic behavior in layered systems.

Resonances or band gaps occur in batteries at the frequency f_n (or a multiple thereof)

$$f_n = \frac{c}{2d} \quad (1)$$

when the wavelength matches the periodicity d of the layering structure, where c is the sound velocity. Frequency-dependent absorption measurements were proposed by Meng et al.^[14] as a method to measure the State of Charge (SoC) by fitting a linear absorption coefficient. In a recent publication by the authors of this work,^[15] it was demonstrated that attenuation comprises a resonant part and the absorption, which can be modeled by a linear-quadratic polynomial. The SoC dependency is more pronounced in the resonant part than in absorption, with the first resonance appearing promising for SoC determination in NMC-graphite systems.

The primary aim of this work is to present and validate the measurable quantities, specifically the ToF and amplitude (group velocity and attenuation), across a broad frequency

[a] S. Feiler, Dr. L. Gold, Dr. S. Hartmann, Dr. G. A. Giffin
Fraunhofer R&D Center Electromobility Fraunhofer Institute for Silicate Research
Neunerplatz 2, 97082 Würzburg (Germany)
E-mail: guinevere.giffin@isc.fraunhofer.de

[b] Dr. G. A. Giffin
Julius-Maximilians-Universität Würzburg (JMU)
Faculty of Chemistry and Pharmacy
Chemical Technology of Materials Synthesis
Röntgenring 11, 97070 Würzburg (Germany)

 Supporting information for this article is available on the WWW under <https://doi.org/10.1002/batt.202400478>

 © 2024 The Authors. *Batteries & Supercaps* published by Wiley-VCH GmbH. This is an open access article under the terms of the Creative Commons Attribution License, which permits use, distribution and reproduction in any medium, provided the original work is properly cited.

range. This article builds on the previous work presented in Ref. [15] and parametrizes a semi-empirical transfer matrix model from direct measurements of the individual cell components. This effectively reproduces the behavior of sound velocity and attenuation over a broad frequency interval, particularly the enhanced group velocity, enhanced attenuation and the SoC-dependent aspect of the resonances. By doing so, potential pitfalls that experimenters might encounter when choosing interrogation frequencies close to a resonance are identified. This contributes to the reliability and accuracy of future experimental work in this area.

The transfer matrix model of a battery is introduced in Sec. *Transfer Matrix Model of a Battery* and parametrized in Sec. *Model Parametrization*. The modeled attenuation and sound velocity are compared to measurements in Sec. *Validation of Battery Tranfer Matrix Model*. A visualization of pulse propagation and the standing waves at the resonances with possible use cases are presented in Sec. *Visualization of Wave Propagation*.

Results and Discussion

Transfer Matrix Model of a Battery

The transfer matrix notation is an elegant mathematical tool used to describe and analyze the behavior of linear systems, particularly those involving the stratified structure of multiple components. Transfer matrices can be utilized to analyze the propagation of sound waves in multi-layered materials. The individual layers may have varying acoustic properties and the transfer matrix helps describe how sound waves are affected as they pass through or are reflected by these layers. Therefore, the transfer matrix provides a mean to calculate the transmission of a system. The transfer matrix formalism employed in this work is inspired by Luce et al.,^[16] who created a computational package for modeling multilayer thin-film optical systems. The model is adapted for acoustic system under normal incident. The phase shifts introduced by individual layers are determined entirely by the previously measured sound velocities in dummy cells (as discussed in Sec. *Model Parametrization*) and the layer thicknesses. Reflection and transmission at the interfaces between layers are calculated using the standard acoustic reflection and transmission coefficients. A key advantage of this semi-empirical method is that it avoids the need for additional theoretical assumptions, e.g., such as the choice between the Biot model and slurry model for electrode treatment.

The transfer matrix T of an acoustic system relates the wave vector Ψ_i to the left of the system to the wave vector Ψ_f to the right of the system, see Figure A.5 in the supporting information (SI):

$$\Psi_i = T\Psi_f \quad (2)$$

$$\begin{pmatrix} \Psi_{i,r} \\ \Psi_{i,l} \end{pmatrix} = \begin{pmatrix} T_{11} & T_{12} \\ T_{21} & T_{22} \end{pmatrix} \begin{pmatrix} \Psi_{f,r} \\ 0 \end{pmatrix} \quad (3)$$

where the wave vector Ψ_i consists of a the incident wave in the rightward direction $\Psi_{i,r}$ and reflected wave in the leftward direction $\Psi_{i,l}$. The transmitted wave vector Ψ_f consists of the exiting wave in the rightward direction $\Psi_{f,r}$. There is no component in the leftward direction on the exiting side due to the absence of any more interfaces capable of causing a reflection. In the transfer matrix method, the acoustic properties of each layer or component are represented as a transfer matrix, and then these matrices are combined to calculate the overall behavior of the acoustic system. The transfer matrix of a multi-layered system can be constructed using propagation matrices P_{M_i} for each material M_i to account for phase-shift and absorption which are followed by an interface matrix $D_{M_i, M_{i+1}}$ that describes the reflection and transmission behavior at the material interface. The propagation matrix P_{M_i} of material M_i is defined as:

$$P_{M_i} = \begin{pmatrix} e^{(ik_{M_i} - \alpha_{M_i})d_{M_i}} & 0 \\ 0 & e^{-(ik_{M_i} - \alpha_{M_i})d_{M_i}} \end{pmatrix} \quad (4)$$

where d_{M_i} is the thickness of the material layer M_i , α_{M_i} is the absorption coefficient and k_{M_i} is the angular wavenumber, defined by the speed of sound c_{M_i} in medium M_i and the measurement frequency f :

$$k_{M_i} = \frac{2\pi}{\lambda} = 2\pi \frac{f}{c_{M_i}} \quad (5)$$

The interface matrix of medium M_i and medium M_{i+1} is defined as:

$$D_{M_i, M_{i+1}} = \frac{1}{t_{M_i, M_{i+1}}} \begin{pmatrix} 1 & r_{M_i, M_{i+1}} \\ r_{M_i, M_{i+1}} & 1 \end{pmatrix} \quad (6)$$

where $r_{M_i, M_{i+1}}$ is the reflection coefficient at the interface of material M_i to material M_{i+1} defined as

$$r_{M_i, M_{i+1}} = \frac{Z_{M_{i+1}} - Z_{M_i}}{Z_{M_i} + Z_{M_{i+1}}} \quad (7)$$

and $t_{M_i, M_{i+1}}$ is the transmission coefficient from material M_i to material M_{i+1} defined as

$$t_{M_i, M_{i+1}} = \frac{2Z_{M_{i+1}}}{Z_{M_i} + Z_{M_{i+1}}} \quad (8)$$

where Z_{M_i} is the acoustic impedance of material M_i , defined as the product of density ρ_{M_i} and sound velocity c_{M_i} :

$$Z_{M_i} = \rho_{M_i} c_{M_i} \quad (9)$$

The transfer matrix of a battery T_{Bat} can be established by multiplying a propagation matrix followed by an interface matrix for every layer shown in Figure 1. The periodic part is represented as:

$$T_{\text{Bat,periodic}} = \prod_{i=0}^{17} [P_{Al} D_{Al,Cat} P_{Cat} D_{Cat,Sep} P_{Sep} D_{Sep,An} P_{An} \\ D_{An,Cu} P_{Cu} D_{Cu,An} P_{An} D_{An,Sep} P_{Sep} D_{Sep,Cat} P_{Cat} D_{Cat,Al}] \quad (10)$$

Together with the non-periodic parts, the transfer matrix of the entire battery cell is formulated as:

$$T_{\text{Bat}} = P_{\text{Pouch}} D_{\text{Pouch},\text{Sep}} P_{\text{Sep}} D_{\text{Sep},\text{Al}} T_{\text{Bat,periodic}} \\ P_{\text{Al}} D_{\text{Al},\text{Sep}} P_{\text{Sep}} D_{\text{Sep},\text{Pouch}} P_{\text{Pouch}} \quad (11)$$

From the definition of the transfer matrix, see eq. 3, the transmitted (rightward) wave can be expressed in terms of the incident (rightward) wave using the $T_{\text{Bat}_{11}}$ matrix element of the transfer matrix T_{Bat} :

$$\Psi_{i,r} = T_{\text{Bat}_{11}} \Psi_{f,r} \quad (12)$$

From this equation, the measurable quantities attenuation and phase shift can be obtained. The ratio of transmitted and incident wave can be obtained by

$$\frac{\Psi_{f,r}}{\Psi_{i,r}} = \frac{1}{T_{\text{Bat}_{11}}} \quad (13)$$

Therefore, the attenuation coefficient, including attenuation from absorption and band gaps, in dB/m by

$$\alpha_{\text{Bat}}(f) = -\frac{1}{L} \log \left[\left| \frac{1}{T_{\text{Bat}_{11}}} \right| \right] 20 \text{dB} \quad (14)$$

The phase shift accumulated by the wave transversing the battery can be expressed by

$$\varphi = \arg(T_{\text{Bat}_{11}}) \quad (15)$$

where \arg is the argument of the complex number $T_{\text{Bat}_{11}}$.

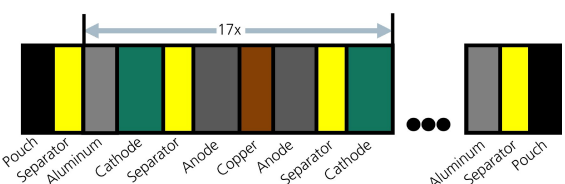


Figure 1. Schematic of the layered lithium-ion battery (LIB) structure. The LIB consists of an outer pouch layer followed by a Z-folded electrode stack, consisting of double-sided graphite-coated copper and NCM-coated aluminum. The outer NCM-coated aluminum is single-sided and has a thicker aluminum foil.

Model Parametrization

To parameterize the model, the thickness and density of the anode, cathode, separator and pouch foil were determined. The speed of sound was measured in mock cells, built from harvested electrodes.

The model parameters were established by disassembling two pristine cells in the fully charged state (100% SoC) and two pristine cells in the completely discharged state (0% SoC) in argon atmosphere. The thickness and density of the individual layers were measured by punching out 16 mm disks. The residues of the dried electrolyte were washed out twice with dimethyl carbonate (DMC). The thickness of the extracted electrodes was measured using a contact sensor (Keyence GT2-H12 K). The thickness of the electrodes was measured outside the glovebox environment. The anodes at 100% SoC reacted with air and yielded an inaccurate thickness measurement. Therefore, the thickness of the anode at 100% SoC was determined by measuring the thickness of the mock cell and deducing the thickness of individual layers from that measurement. The active material of one anode and one cathode disk was scraped off and the thickness of the copper and aluminum was measured. These measurements were corroborated with the thickness measurement at the uncoated part of the current collector. The thickness of the active material was derived by subtracting the thickness of the current collector. The discs were also weighed to determine the densities of the anode, cathode, separator and pouch foil. The results of the thickness and density measurement are summarized in Table 1.

Mock cells with double-sided coated cathodes, double-sided coated anodes (at 0% and 100% SoC, respectively), pouch foils

Table 1. Parameters of the layers of the 12 Ah lithium-ion cell investigated. Sound velocity $c[\text{m/s}]$, density $\rho[\text{kg/m}^3]$, acoustic impedance $Z[\text{GRayl}]$, thickness $d[\mu\text{m}]$, number of components in original cell n . Except for the density and sound velocity of aluminum and copper, all parameters were measured in this work. The sound velocity is calculated from a weighted average of the mock cells. The discrepancies between measured and calculated thickness are explained in the text.

Material	c	ρ	Z	d	n
Copper	4660 ⁽¹⁷⁾	8940 ⁽¹⁷⁾	41.7	11.3	17
Aluminum	6250 ⁽¹⁸⁾	2700 ⁽¹⁸⁾	16.9	14.7	16
Aluminum outer	6250	2700	16.9	45.8	2
Separator	1605	696	1.12	14.7	37
Pouch	1942	1406	2.73	155.0	2
Anode (0% SoC)	1625	1579	2.57	80.0	34
Anode (100% SoC)	1859	1498	2.79	84.3	34
Cathode (0% SoC)	1447	2928	4.24	59.9	34
Cathode (100% SoC)	1310	2879	3.77	57.9	34
Cell (0% SoC)					
measured	1475			6326	
calc.				6130	
Cell (100% SoC)					
measured	1553			6432	
calc.				6208	

and separators were built to determine the sound velocity of the individual components. The number of layers in each type of mock cell is shown in Figure 2. The components were sealed in a pouch bag and filled with a adequate coupling agent to allow ultrasonic transmission. For the porous battery materials, the mock cells were filled with electrolyte (LP57) to act as a coupling agent between layers and facilitate US propagation. Canola oil was used for the mock cell made purely out of pouch.

The thickness of the mock cells was measured when braced at 25 kPa inside the setup by a laser dilatometer. More details on the individual measurements can be found in Sec. A.2 in the SI. The thickness of the mock cells is in good agreement with the calculated thickness derived from the sum of the individual components, ref. Table S2 in the SI. The measured thickness of the pouch foil stack was a bit larger, possibly due to residual canola oil between the layers, while that of the separator was a bit lower, possibly due to the high compressibility of the separator when measured at 25 kPa vs the unbraced measurement of a single separator sheet with the contact sensor. For the anodes at 100% SoC, the thickness of the individual layer could not be determined by direct measurement (as mentioned above), therefore was calculated from the thickness of the mock cell stack by subtracting the known thickness of the other components.

Sound velocity measurements of the mock cells were conducted according to Sec. A.1. The results are shown in Figure 2. The sound velocity of the individual layers of interest was calculated by assuming that the sound velocity of the stack is a weighted average of the individual components. For example, when considering two media with the thicknesses x_1 and x_2 and the sound velocities of v_1 and v_2 , then the sound velocity v of the two media combined is:

$$v = \frac{v_1 v_2 (x_1 + x_2)}{x_1 v_2 + x_2 v_1} \quad (16)$$

The resulting sound velocities for the layers of interest are summarized in Table 1, while more details on the individual mock cells can be found in Sec. A.2 in the SI. From Table 1, it becomes obvious that a greater total thickness of the battery cell is measured than calculated from the sum of the individual components. Part of this difference might be attributed to the aging of the battery cell used for the US measurements vs the pristine cells that were disassembled. While conducting the experiments, the cell was cycled and held at high SoCs for long periods of time, which probably lead to degradation, i.e. lithium plating or SEI formation. Degradation leads to an increase in thickness in this cell type.^[19] Small cell to cell deviations and variations in the applied pressure during thickness measurements could also have contributed to the discrepancies in cell thickness. The results of the density and sound velocity measurements have been compared to existing literature. Graphite has a crystal density of 2260 kg/m³.^[20] Therefore a measured density of 1579 kg/m³ would yield a realistic porosity of $\approx 30\%$. Moiseev et al.^[21] report tap densities (powder compact density) of 2.9(3.8)kg/dm³ for single crystal and 2.3(2.7)kg/dm³ for polycrystalline NCM811, making the measured value of 2.9 kg/dm³ seem realistic. The sound velocity measurements are hard to compare since they are usually reported either for individual particles or bulk materials. The sound velocity in porous materials depends heavily on pore size and porosity.^[22] Additionally, the liquid electrolyte in the pores leads to a further decrease in sound velocity.^[23] Nonetheless, the general differences between lithiated and delithiated material can be confirmed. The Young's modulus of NCM decreases during delithiation.^[24] Consequently, the 100% SoC cathode should exhibit a lower sound velocity compared to the 0% SoC cathode, as observed in Figure 2. Likewise, the Young's modulus of graphite increases during lithiation,^[25] explaining the larger sound velocity of the anodes at 100% SoC (see, Figure 2).

The sound velocity and density of the graphite and NCM were linearly extrapolated between 0% and 100% SoC to be used in the model. A simplification was made wherein the

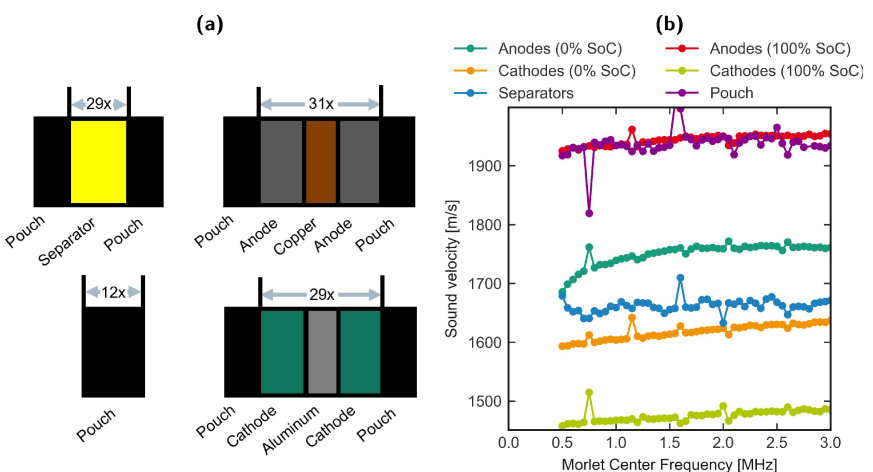


Figure 2. Sound velocity measurements of individual cell components. a) Schematic of the mock cells. b) Sound velocity of the mock cells at various Morlet center frequencies. Larger sound velocities are measured at higher center frequencies due the dispersive nature of an attenuating medium.

sound velocity of the individual cell components remains constant across frequencies but varies only with different SoCs.

The absorption was modeled by the alpha parameters measured in Ref. [15].

$$\alpha(f, \text{SoC}) = a(\text{SoC})f + b(\text{SoC})f^2 \quad (17)$$

Since no individual absorption coefficients were measured for the individual components, the same absorption coefficient was assumed for graphite, NCM and separator. The pouch bag and current collectors were assumed to have negligible absorption since the absorption coefficient is at least an order of magnitude smaller for metals than for the porous active material and separator.^[26]

Validation of Battery Transfer Matrix Model

In this section, the attenuation and sound velocity of the ultrasound spectroscopy measurement presented in Ref. [15] is compared to the predicted attenuation and sound velocity of the model.

Comparison of Measured and Modeled Attenuation

One measurable quantity in ultrasound transmission measurements is the amplitude of the pulse traversing the battery. The amplitude is affected by the attenuation of the battery, which can be calculated by dividing the Fourier Transform of the pulse through the setup with battery by the Fourier Transform $U_{\text{sample}}(f)$ of the pulse through the empty setup $U_{\text{empty}}(f)$. Taking the logarithm of this fraction and dividing by the thickness L of the battery yields the attenuation coefficient in db/mm:

$$\alpha_{\text{bat}}(f) = -\frac{1}{L} \log \left[\left| \frac{U_{\text{sample}}(f)}{U_{\text{empty}}(f)} \right| \right] 20 \text{ dB} \quad (18)$$

A more detailed derivation is given in Ref [15]. When conducting amplitude or attenuation measurements, the center frequency of the interrogation pulse has to be chosen with great care. When the wavelength matches the periodicity of the cell, see Figure 3b, constructive interference of the reflected waves occurs, resulting in reduced transmission. This phenomenon is known as a band gap. In the case of a finite sample, a pulse may still be transmitted even if its frequency lies within the band gap, albeit with exponential attenuation.

The attenuation obtained in the ultrasound spectroscopy measurement presented in Ref. [15] are plotted in Figure 3a. The attenuation inside the second resonance was too large to measure any transmitted pulse. The measured noise sets a lower limit on the attenuation inside the second resonance. Figure 3c shows the resulting attenuation from the model, i.e. the evaluation of eq. 14. It can be observed that the model and data are qualitatively similar. The two resonances are clearly distinguishable from the absorption background and the magnitude of the attenuation at the first resonance frequency decreases for increasing SoCs. This resonance occurs because the graphite-copper interface is much more reflective than the NCM-aluminum interface at low SoCs. The higher reflectivity is due to a larger difference in acoustic impedance, as shown in Table 1. As the SoC increases, the acoustic impedance of graphite increases, thereby decreasing the difference in acoustic impedance at the graphite-copper interface and reducing its reflectivity. At the same time, the acoustic impedance of NCM decreases, thereby increasing the difference in acoustic impedance at the NCM-aluminum interface, making it more reflective. These two effects cause the resonance to weaken as the SoC increases, eventually resulting in the disappearance of

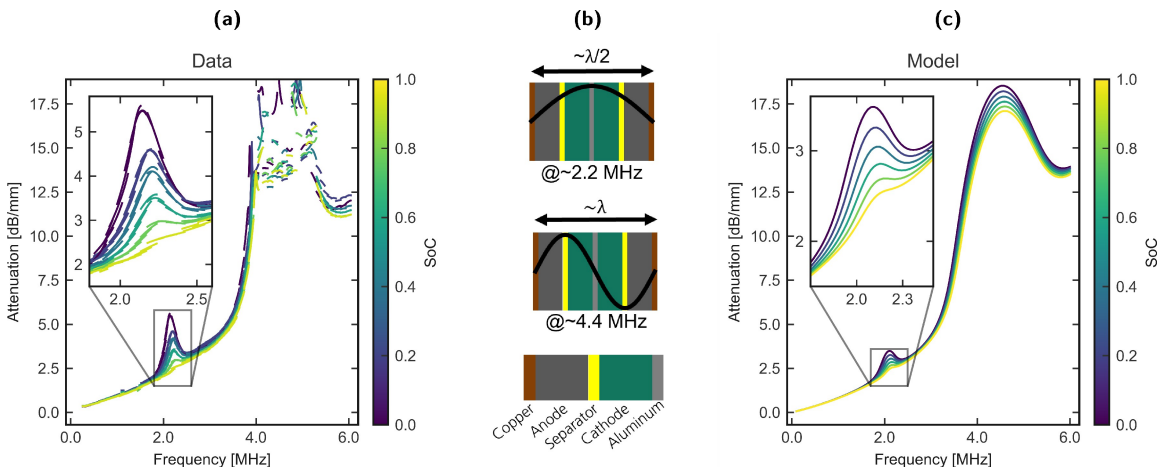


Figure 3. Comparison of the a) modeled and c) measured attenuation coefficient across frequencies. The modeled attenuation is in good agreement with the measurements. At the resonances depicted in b), the wavelength matches the periodicity of battery layers and the attenuation is enhanced due to constructive interference in reflection. The magnitude of the attenuation at the resonance frequencies decreases for increasing SoCs due to changes in the reflectivity of the NCM-aluminum and graphite-copper interfaces caused by changes in acoustic impedance of the active material at different degrees of lithiation. a) and b) are licensed under CC BY 4.0 DEED Creative Commons Attribution 4.0 International License by Feiler et al.^[15] Small changes were made to a).

the resonance at 100% SoC. The SoC dependency of this resonance was proposed as a SoC estimation method in Ref. [15]. The model effectively describes the observed effects, albeit with slight deviations. The resonances of the model are shifted to slightly lower frequencies implying that the assumed sound velocities for parameterization were underestimated. This discrepancy could arise from the simplification of assuming a constant sound velocity across frequencies during the modeling process or from inaccuracies in calculating the sound velocities of NCM and graphite based on a weighted average with the current collectors, as shown in Eq. 16. The first resonance in the model is also smaller in magnitude than that measured. This again is caused by inaccuracies of the sound velocity leading to offset in acoustic impedance and therefore reflectivity of the interfaces.

Comparison of Measured and Modeled Sound Velocity

The second measurable quantity in ultrasound transmission measurements is the time it takes a pulse to traverse the sample or ToF. The length of the sample divided by the ToF is the group velocity of the pulse. An illustration how the ToF can be measured by calculating the cross-correlation of a signal passing through the empty setup and a signal passing through the setup with battery is given in Sec. A.1 in the SI. This work shows that the center frequency of the pulse has to be selected with great care for ToF measurements. Similar to band gaps in solid-state physics, there is dispersion in the vicinity of band gaps. The group velocity is lower close to the band gap. Inside the band gap of a finite sample, the group velocity is enhanced.^[27,28] The measured group velocity from Ref. [15] is plotted as a function of frequency and SoC in Figure 4a. Inside the second band gap (4 MHz to 5 MHz), no measurable signal was received due to the high attenuation. The dispersion can be derived from the model introduced here by taking a closer

look at the wavenumber k , obtainable from the phaseshift in eq. 15:

$$k = \arg(T_{Batt_{11}})/L \quad (19)$$

The phase velocity $v_{ph}(f)$ at a given frequency f is given by:

$$v_{ph}(f) = \frac{\omega}{k} = \frac{f}{2\pi k} \quad (20)$$

and the group velocity $v_{gr}(f)$ at a given frequency f is given by:

$$v_{gr}(f) = \frac{\partial \omega}{\partial k} = \frac{1}{2\pi} \frac{\partial f}{\partial k} \quad (21)$$

$$v_{gr}(f) = \frac{\partial \omega}{\partial k} = \frac{L}{2\pi} \frac{\partial f}{\partial \arg(T_{Batt_{11}})} \quad (22)$$

The dispersion relation k over f and phase velocity v_{ph} are shown Figure A.3 and Figure A.4 in the SI. The group velocity v_{gr} is shown in Figure 4b. Since the sound velocities of the individual cell components were assumed to be free of dispersion in the model, the apparent dispersion of the group velocity is solely an emergent property of the layered structure. It can be seen that the modeled group velocity effectively captures all the features that can be observed in the measured data. This includes the decrease in v_{gr} at the edges of the band gap and the increase inside the first band gap. These large variations might explain the discontinuities observed in sound velocity measured by Gold et al.^[11] As the battery is charged, the v_{gr} gradually decreases in the first band gap. In contrast to the experiment, the first band gap in the model never completely disappears. This is likely attributed to the aforementioned imperfections in the parametrization of the sound velocity.

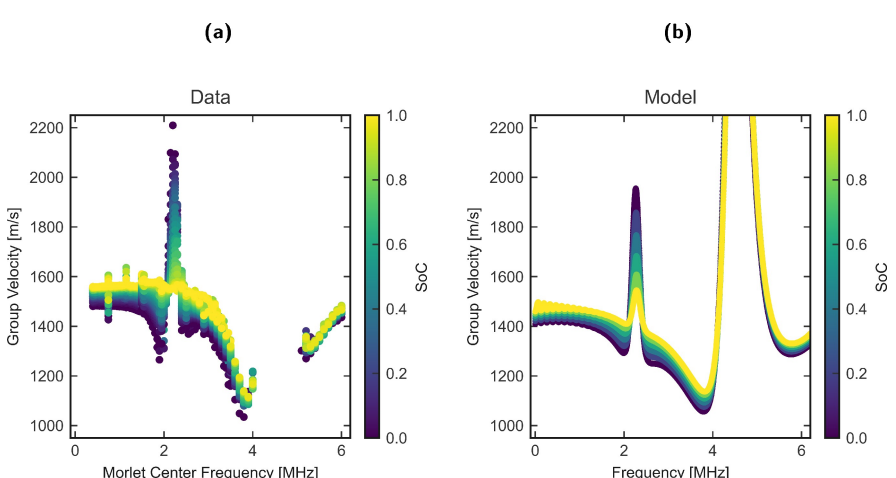


Figure 4. Comparison of the a) modeled and b) measured group velocity across frequencies. The sound velocity within the second band gap could not be measured due to high attenuation. The modeled group velocity is in good agreement with the measurements. At the band gaps, the group velocity is enhanced; left and right of the band gaps, the group velocity is decreased. This effect is known from solid-state physics. The effect of the first band gap decreases for increasing SoCs due to changes in the reflectivity of the NCM-aluminum and graphite-copper interfaces. These are caused by changes in acoustic impedance of the active material at different degrees of lithiation. The measurement of the group velocity was conducted in Ref. [15].

In summary, it can be seen that modeling the layered structure with a transfer matrix can successfully describe the attenuation behavior and dispersion of the battery cell including the resonances. Therefore, it can serve as a simple model to extrapolate to even higher frequencies, e.g. to pick an ideal frequency when choosing a frequency for scanning acoustic microscopy in the two digit MHz range. This model could potentially serve as a framework for a fitting model with the potential to mechanically characterize the individual components of a cell from a single spectroscopy measurement. Its applications would be similar to those of electrochemical impedance spectroscopy but are directed toward mechanical parameters. This could allow the tracking of changes in thickness, stiffness and density of all the individual cell components and therefore be sensitive to, e.g., aging effects due to film formation.

Visualization of Wave Propagation

The propagation of Morlet wavelets through the LIB is animated to illustrate the effects described up to this point and specific frequencies of interest where standing waves form are presented.

To compute the amplitude and phase of the pressure waves at arbitrary positions within the layered structure, the transfer matrix was partitioned into right and left components relative to the point of interest, as presented in Sec. A.5 in the SI. With the partitioning, the amplitude and phase of the pressure wave can be calculated at any position and time in the cell and delay lines, see eq. 37. The pressure modulation caused by a Morlet pulse can be constructed by Fourier synthesis, as is explained in Sec. A.6. For this section, the transfer matrix model was parameterized using the cell parameters at 0% SoC. Figure 5a shows the resulting attenuation of the battery model. The center frequency of the modeled Morlet at 1.2 MHz is indicated by the red line and a bandwidth (FWHM) of 600 kHz was used. The pressure modulation caused by the pulse was calculated from eq. 43 for each layer inside the battery and the two delay lines. The pressure modulation is plotted with increasing time in Figure 5b-d. The dashed arrows indicate the direction of the wave. An animation can be viewed in the SI (Fig5.1_1.2 MHz.mp4). The reflected and transmitted signals at this frequency, which is well below the first resonances of the cell, show no visible distortion. This observation highlights that frequencies outside the resonant frequencies can be effectively utilized for ToF measurements. Additionally, only a small portion of the signal gets reflected, suggesting that absorption predominantly causes the attenuation. Hence, this frequency is well suited for measuring the absorption characteristics of the battery materials. A Morlet with center frequency at the first band gap was also animated (Fig5.2_2.1 MHz.mp4, see SI). The reflected and transmitted signal at this band gap are visibly distorted, which could cause problems in ToF evaluation algorithms. In addition, a large portion of the signal is reflected. This underscores the importance of selecting an appropriate frequency, as an unsuitable choice could introduce undesirable

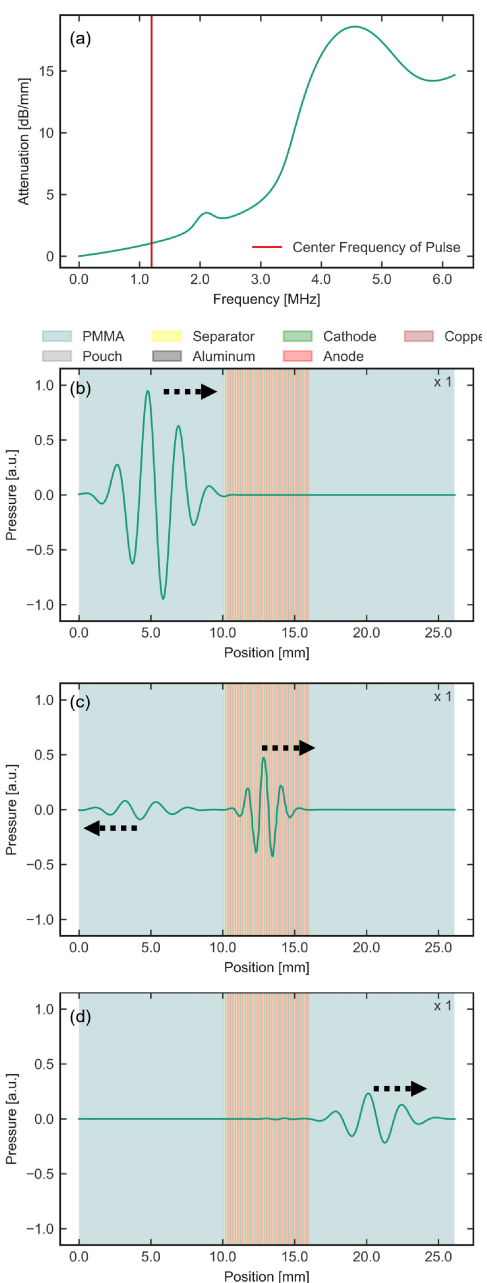


Figure 5. Model of a Morlet pulse traversing a battery cell. a) shows the attenuation of the transfer matrix battery model at 0 % SoC. The red line marks the pulse's center frequency at 1.2 MHz. b), c), d) illustrate the pressure modulation with increasing time. An animation can be viewed in the SI (Fig5.1_1.2 MHz.mp4).

effects in ToF and amplitude measurements. Between the resonances, a Morlet with center frequency 3.0 MHz (Fig5.3_3.0 MHz.mp4, see SI) was animated. Although, the reflected and transmitted signals exhibit no visible distortion, the signal is heavily attenuated due to the linear quadratic increase in absorption with frequency (note the x100 magnification of the signal in the right PMMA delay line). At the second band gap at (Fig5.4_4.4 MHz.mp4, see SI), the full effect of the band gap can be observed. At this frequency the reflections caused at the

metal layers constructively interfere, heavily suppressing transmission. Almost the entire wave gets reflected. This explains why no signal could be measured in this frequency range.

At and around the resonance frequencies when the wavelength of the acoustic wave aligns with the periodicity of the layered structure, standing waves form. These standing waves have regions of high pressure variations (antinodes) and low pressure variations (nodes), putting a lot of stress on materials located in the antinodes and minimal stress on materials located in the nodes. This phenomenon could open up opportunities for targeted cell treatments using high-intensity ultrasound. In the frequency range under investigation, standing waves form inside the two band gaps. For the visualization of the standing waves the absorption of the model was set to zero. Absorption would lead to an exponential decay of sound pressure which would overlay the effects under investigation in this section. To visualize the standing waves, the maximum pressure of the sound wave at every position inside the cell is depicted in Figure 6. The pressure is given by eq. 37 and derived in Sec. A.5 in the SI. In the top panels of Figure 6a-f the attenuation of the cell is shown with a marker indicating the excitation frequency. A continuous sine excitation was used. Six frequencies of interest are showcased, representing left, middle,

and right positions relative to the observed resonances. The pressure profile at the middle of the resonance shows an exponential decay, see Figure 6b and 6e. Note that this is not due to absorption but is an emergent property of the layered structure, i.e. the band gap. Within the band gap transmission is exponentially attenuated. At the left edge of the first resonance (see Figure 6a), the maximum pressure manifests in the anode, while pressure nodes occur in the cathode. Conversely, at the right edge of the first resonance (refer to Figure 6c, the maximum pressure is observed in the cathode with standing wave nodes in the anode. At the left edge of the second resonance (see Figure 6d), the maximum pressure is observed in the separators, with nodes in the metals. Conversely, at the right edge of the second resonance (refer to Figure 6f), the maximum pressure is found in the metals, with nodes in the separators. These effects offer potential applications across various scenarios utilizing high-intensity ultrasound. For example, one could leverage a mode featuring pressure maxima within the separator to facilitate self-healing of the cell. This could involve breaking lithium dendrites that may otherwise penetrate the separator or clearing clogged pores.

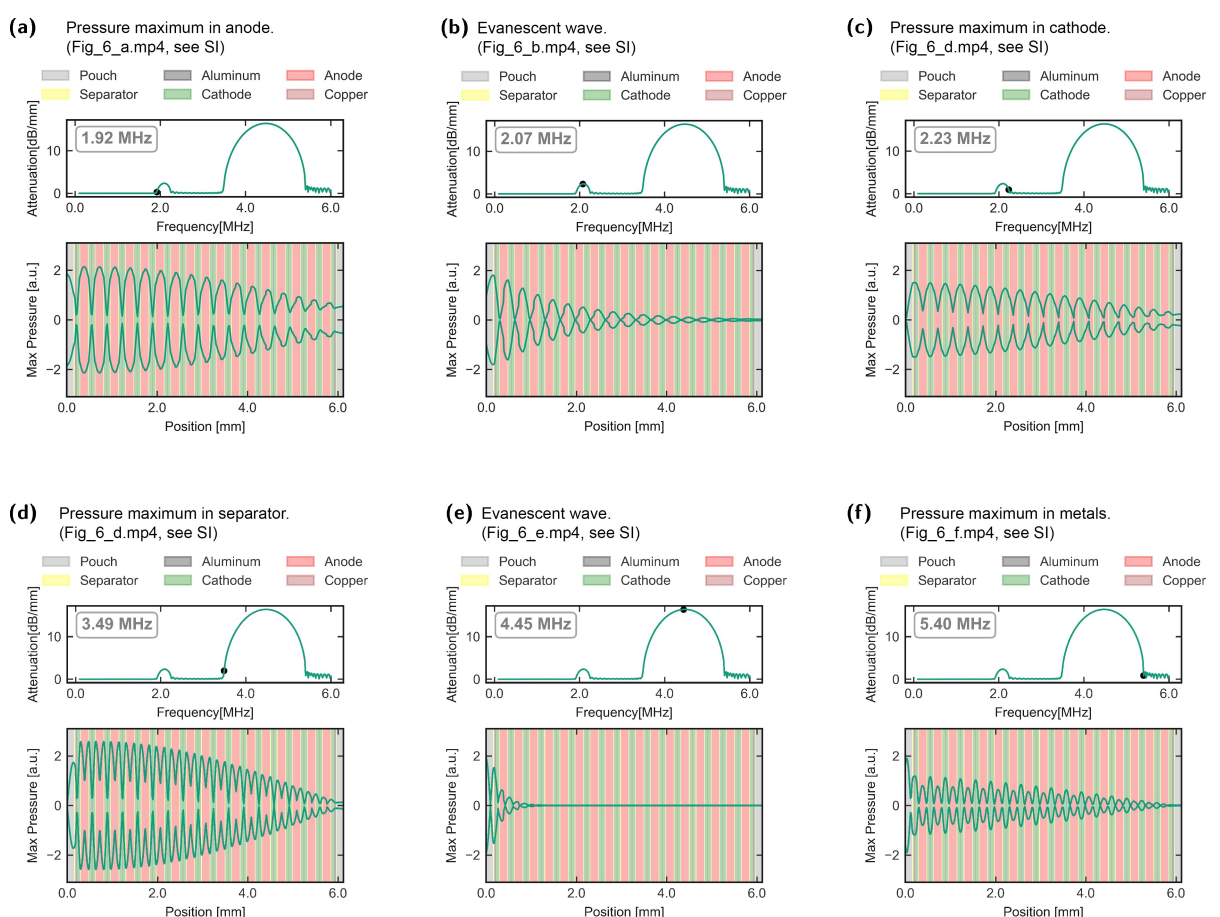


Figure 6. Maximum acoustic pressure for standing waves forming around resonances inside the battery cell under single-frequency excitation. Absorption of the transfer matrix battery model was set to zero. The attenuation is depicted in the upper panels, with a marker indicating the frequency of the sine excitation. The location of nodes and antinodes of the pressure wave could potentially be utilized to target specific cell components with high intensity ultrasound. Animations of the standing waves can be viewed in the SI (see references in the individual captions).

Conclusions

A 1D transfer matrix model of a battery was presented and parametrized using individual cell components from disassembled cells at 0% SoC and 100% SoC. The model enables the two measurable quantities from ultrasound transmission measurements to be calculated: the group velocity and attenuation of the battery. The calculated attenuation is in good agreement with the measurements. The attenuation is enhanced at the band gaps where the wavelength matches the periodicity of battery layers. This phenomenon arises from constructive interference of the reflected waves increasing the overall reflection, thereby reducing transmission and consequently increasing attenuation. The modeled group velocity is also in good agreement with the measurements. Left and right of the resonances, the group velocity is lower while inside the group velocity is enhanced. The decrease of the band gaps (decreasing its effect on sound velocity and attenuation) for increasing SoCs was also reproduced by the model. The distortions of attenuation and sound velocity in the vicinity of the bandgaps emphasizes the importance of selecting a suitable interrogation frequency for ultrasound investigations in lithium-ion batteries. The model offers the potential for fitting the US spectroscopy data, providing immediate determination of the thickness and Young's modulus of all individual cell components. This capability allows, e.g., aging effects between the anode and cathode to be distinguished. The wave propagation inside the battery was visualized using the model. For a propagating Morlet pulse, the deformation of reflected and transmitted pulses at the first resonance and the almost total reflection at the second resonance were observed. Standing waves were observed to form at four frequencies, located at the edges of the two resonances. Pressure antinodes were identified in the anodes, cathodes, current collectors, and separators, respectively. These frequencies could be employed in high-intensity ultrasound applications aimed at individual cell components, such as specifically targeting the separators. This approach could potentially break lithium dendrites that might otherwise penetrate the separator or clear clogged pores and therefore facilitate cell healing.

Experimental

Battery Specifications

LIBs (SLPB065070180, Kokam Co., Ltd) with a nominal capacity of 12 Ah were utilized. These batteries feature a graphite anode and a nickel-rich NCM cathode. Although the exact composition of the electrolyte is not disclosed in the data sheet, it is understood to consist of lithium hexafluorophosphate (LiPF_6) dissolved within a blend of ethylene carbonate (EC) and ethyl methyl carbonate (EMC). The electrodes' active area measures 67 mm \times 165 mm.

Experimental Setup

In Figure 7, a schematic representation of the experimental setup is depicted. The cell was subjected to an external pressure of 25 kPa,

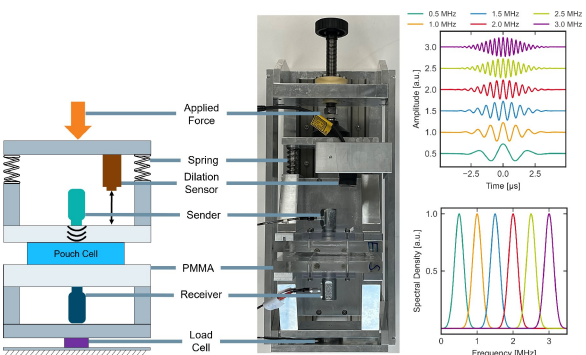


Figure 7. Diagram and image of the experimental configuration and example excitation signals. The cell is secured between two polymethyl methacrylate (PMMA) plates, with transducers mounted on the bracing plates. Pressure and cell thickness are continuously monitored. On the right, example Morlet excitation signals are presented in both the time and frequency domains. Licensed under CC BY 4.0 DEED Creative Commons Attribution 4.0 International License by Feiler et al.^[15]

maintained within a ± 1 kPa range through the utilization of two springs (model number 13000, with a spring constant of 17.65 N/mm, sourced from SODEMANN Industrifjedre A/S). Accurate measurement of the force exerted on the battery cell was achieved using a force sensor (KM38-1 kN load cell, manufactured by ME-Systeme GmbH). To ensure uniform pressure distribution, the cells were positioned between two PMMA plates, each 15 mm thick, functioning as both delay lines and pressure distribution media. PMMA was selected due to its favorable acoustic properties, with its acoustic impedance closely matching that of LIBs, thereby ensuring optimal coupling and minimizing losses from reflections. Two transducers were affixed to the PMMA bracings and acoustically coupled using canola oil. Canola oil was also used as a coupling agent at the battery-PMMA interface.

Ultrasonic Measurements

The thickness of the samples was measured using a laser dilation sensor (IL-S065, KEYENCE DEUTSCHLAND GmbH) connected to an amplifier unit (IL-1000, KEYENCE DEUTSCHLAND GmbH). Morlet wavelets were employed for the measurements, characterized by the equation:

$$M(t) = \pi^{-0.25} \exp(i\pi f_0 t) \exp\left(-\frac{1}{2} \frac{t^2}{\sigma^2}\right) \quad (23)$$

The Morlet waveforms were generated with a bandwidth (full width half max (FWHM)) of 294 kHz corresponding to pulse width (FWHM) of 3 μ s. During spectroscopy, the center frequency was adjusted in 50 kHz increments. Two V609 from Olympus, with a nominal center frequency of 5 MHz, a bandwidth (FWHM) of 74% and a diameter of 13 mm were used as transducers. For generating Morlet waveforms, an arbitrary waveform generator TGP3151 (Aim TTI) was interfaced via Python VISA. The signals were amplified by a broadband high-frequency amplifier Hubert A1020-75-250 to a maximum of 100 V. Signal acquisition was conducted using an oscilloscope (WaveSurfer HD by Teledyne LeCroy) at a sampling rate of 500 MS/s, with signals averaged over 1024 shots.

Acknowledgements

The authors gratefully acknowledge the funding of this work by the Federal Ministry of Education and Research (BMBF) of Germany in the project MAD3AM4Life (grant number 03XP0327). The authors also want to thank the members of the Fraunhofer R&D Center Electromobility for fruitful discussions and scientific support and Alexander Wittye for the construction and the improvement of the measurement setup. Open Access funding enabled and organized by Projekt DEAL.

Conflict of Interests

The authors declare no conflict of interest.

Data Availability Statement

The data that support the findings of this study are available from the corresponding author upon reasonable request.

Keywords: Lithium-ion battery • Ultrasonic resonance • Ultrasound spectroscopy • Layered structure • State of charge

- [1] A. G. Hsieh, S. Bhadra, B. J. Hertzberg, P. J. Gjeltema, A. Goy, J. W. Fleischer, D. A. Steingart, *Energy Environ. Sci.* **2015**, *8*, 1569.
- [2] L. Gold, T. Bach, W. Virsik, A. Schmitt, J. Müller, T. E. Staab, G. Sextl, *J. Power Sources* **2017**, *343*, 536.
- [3] P. Ladpli, F. Kopsaftopoulos, F.-K. Chang, *J. Power Sources* **2018**, *384*, 342.
- [4] K. W. Knehr, T. Hodson, C. Bommier, G. Davies, A. Kim, D. A. Steingart, *Joule* **2018**, *2*, 1146.
- [5] C. Bommier, W. Chang, J. Li, S. Biswas, G. Davies, J. Nanda, D. Steingart, *J. Electrochem. Soc.* **2020**, *167*, 020517.
- [6] Y. Wu, Y. Wang, W. K. C. Yung, M. Pecht, *Electronics* **2019**, *8*, 751.
- [7] J.-Y. Kim, J.-H. Jo, J.-W. Byeon, *Microelectron. Reliab.* **2020**, *114*, 113859.
- [8] M. C. Appleberry, J. A. Kowalski, S. A. Africk, J. Mitchell, T. C. Ferree, V. Chang, V. Parekh, Z. Xu, Z. Ye, J. F. Whitacre, S. D. Murphy, *J. Power Sources* **2022**, *535*, 231423.
- [9] C. Bommier, W. Chang, Y. Lu, J. Yeung, G. Davies, R. Mohr, M. Williams, D. Steingart, *Gell Reports Physical Science* **2020**, *1*, 100035.
- [10] D. Wasylowski, N. Kisseler, H. Ditler, M. Sonnet, G. Fuchs, F. Ringbeck, D. U. Sauer, *J. Power Sources* **2022**, *521*, 230825.
- [11] L. Gold, T. Herzog, F. Schubert, H. Heuer, G. A. Giffin, *Energy Technol.* **2023**, *11*, 2200861.
- [12] M. Huang, N. Kirkaldy, Y. Zhao, Y. Patel, F. Cegla, B. Lan, *J. Energy Storage* **2022**, *50*, 104585.
- [13] X.-I. Wang, Y. Lyu, G.-r. Song, L.-h. Zhang, C.-f. He, *Theoretical Analysis of Ultrasonic Reflection/Transmission Characteristics of Lithium-Ion Battery*, IEEE **2021**.
- [14] K. Meng, X. Chen, W. Zhang, W. Chang, J. Xu, *J. Power Sources* **2022**, *547*, 232003.
- [15] S. Feiler, L. Gold, S. Hartmann, G. A. Giffin, *Batteries & Supercaps* **2024**, *7*, e202400212.
- [16] A. Luce, A. Mahdavi, F. Marquardt, H. Wankerl, *J. Opt. Soc. Am. A* **2022**, *39*, 1007.
- [17] J. Krautkrämer, H. Krautkrämer, *Ultrasonic testing of materials*, Springer-Verlag, Berlin and Heidelberg, 4th fully revised edition, translation of the 5th revised german edition edition **1990**.
- [18] G. L. Workman, D. Kishoni, P. O. Moore (Editors), *Ultrasonic testing*, volume Vol. 7 of *Nondestructive testing handbook*, American Society for Nondestructive Testing, Columbus, Ohio, 3. ed. edition **2007**.
- [19] S. Feiler, P. Daubinger, L. Gold, S. Hartmann, G. A. Giffin, *Batteries & Supercaps* **2023**, *6*, e202200518.
- [20] R. Mo, X. Tan, F. Li, R. Tao, J. Xu, D. Kong, Z. Wang, B. Xu, X. Wang, C. Wang, J. Li, Y. Peng, Y. Lu, *Nat. Commun.* **2020**, *11*, 1374.
- [21] I. A. Moiseev, A. A. Savina, A. D. Pavlova, T. A. Abakumova, V. S. Gorshkov, E. M. Pazhetnov, A. M. Abakumov, *Energy Advances* **2022**, *1*, 677.
- [22] G. A. Lushnikov, I. G. Popova, V. N. Mustafina, V. Y. Tsarev, *Refractories* **1974**, *15*, 325.
- [23] M. A. Biot, *Theory of Propagation of Elastic Waves in a Fluid-Saturated Porous Solid. I. Low-Frequency Range*, volume **28** **1956**.
- [24] R. Xu, H. Sun, L. S. de Vasconcelos, K. Zhao, *J. Electrochem. Soc.* **2017**, *164*, A3333.
- [25] Y. Qi, H. Guo, L. G. Hector, A. Timmons, *J. Electrochem. Soc.* **2010**, *157*, 558.
- [26] K. Ono, *Appl. Sci.* **2020**, *10*, 2230.
- [27] M. de Dios-Leyva, J. C. Drake-Perez, *J. Appl. Phys.* **2011**, *109*, 103526.
- [28] G. Diener, *Phys. Lett. A* **1996**, *223*, 327.

Manuscript received: July 12, 2024

Revised manuscript received: September 12, 2024

Version of record online: November 16, 2024